Variation of ice microphysical properties with temperature and humidity at tops of convective clouds

Bastiaan van Diedenhoven[1]

[1]Columbia University / NASA Goddard Institute for Space Studies

November 22, 2022

Abstract

A better understanding of the many interacting processes governing the evaluation of ice in natural clouds is required to improve the representation of ice clouds in global circulation models. Recent studies suggest a dominant role of vapor growth processes in determining the temperature dependence of cloud top ice sizes and shapes. Using airborne cloud remote sensing along with reanalysis data, here we show that observed cloud top ice effective radii and estimated normalized growth rates at cloud top highly correlate with an approximately linear relationship, which is consistent with a conceptual model also presented. Furthermore, significant differences in crystal shape characteristics and scattering asymmetry parameters are found between sub- and super-saturated cloud tops over ocean, although not over land. These results provide valuable observational targets for studying ice formation and evolution processes using models, while also helping interpretation of satellite observations of ice microphysical properties at cloud tops.

Variation of ice microphysical properties with temperature and humidity at tops of convective clouds

B. van Diedenhoven[1,2]

[1]Columbia University, 2880 Broadway, New York, NY
[2]NASA GISS, 2880 Broadway, New York, NY

Key Points:

- Cloud top ice effective radii are shown to highly correlate with normalized ice vapor growth rates at cloud top conditions
- Over ocean, observed cloud-top crystal properties differ significantly between sub- and supersaturated conditions
- A conceptual model based on basic growth theory and ice properties is consistent with these observations

Corresponding author: Bastiaan van Diedenhoven, bv2154@columbia.edu, bvandiedenhoven@gmail.com

Abstract

A better understanding of the many interacting processes governing the evaluation of ice in natural clouds is required to improve the representation of ice clouds in global circulation models. Recent studies suggest a dominant role of vapor growth processes in determining the temperature dependence of cloud top ice sizes and shapes. Using airborne cloud remote sensing along with reanalysis data, here we show that observed cloud top ice effective radii and estimated normalized growth rates at cloud top highly correlate with an approximately linear relationship, which is consistent with a conceptual model also presented. Furthermore, significant differences in crystal shape characteristics and scattering asymmetry parameters are found between sub- and super-saturated cloud tops over ocean, although not over land. These results provide valuable observational targets for studying ice formation and evolution processes using models, while also helping interpretation of satellite observations of ice microphysical properties at cloud tops.

Plain Language Summary

The sizes and shapes of ice crystals in cold clouds influence how these clouds evolve and how much sunlight they reflect. Ice crystal shapes and sizes are affected by numerous interacting physical processes. A better understanding on the relative importance of each of these processes is key to improve the representation of ice clouds in climate models. Recent work suggests that the variation of ice crystal shapes and sizes is largely determined by the relatively simple process of ice crystals growing directly from water vapor. Here we use data from a remote sensor mounted on a high-altitude aircraft to infer information about ice crystal sizes and shapes at the tops of convective clouds as a function of top height. By combining this data with water vapor information from a model, we show that the ice crystal sizes highly correlate with ice growth rates predicted by a simple conceptual model based on ice growing directly from water vapor. Furthermore, we find that ice crystal shapes differ significantly in tops where vapor growth is expected compared to where ice is expected to sublimate. These results can help improve ice cloud modeling and the interpretation of satellite observations of ice clouds.

1 Introduction

The sizes and shapes of ice crystals in cold clouds influence the clouds' evolution and radiative properties (Russotto et al., 2016; A. A. Jensen et al., 2018; Van Diedenhoven & Cairns, 2020). In turn, the variation of ice crystal sizes and shapes within clouds are determined by a complex interaction between ice microphysics and dynamic and thermodynamic properties of the atmosphere (Bailey & Hallett, 2004). A better understanding of the many interacting processes governing the formation of complex mixtures of ice of various shapes and sizes in natural ice clouds is required to improve the representation of ice clouds in global circulation models modeling current and future climates (Waliser et al., 2009; Zelinka et al., 2020; Gasparini et al., 2021). In recent work using satellite retrievals over thick ice clouds globally (van Diedenhoven et al., 2020, VD2020 hereafter), we found that systematic variations of ice size and shape with cloud top temperature show a remarkable agreement with simplified ice crystal vapor growth theory and in situ and laboratory data. This agreement suggests that the temperature dependence of the cloud top ice sizes and shapes could be dominated by the vapor growth process and that ice particle distributions observed at cloud top have generally been subjected to depositional growth for a uniform amount of time at average conditions similar to the observed cloud top, which is somewhat surprising given the many processes involved and the large variation in dynamical variables.

At low temperatures, ice growth rates generally increase with temperature, but they display a maximum at a certain temperature above which they decrease again (Pruppacher & Klett, 1997). This profile is largely determined by, on the one hand, the vapor pressure over ice increasing with temperature and, on the other hand, the relative humidity with respect to ice, which generally decreases with temperature. To relate average cloud top ice crystal sizes to vapor growth rates, VD2020 used the rather *ad hoc* assumption that the relative humidity at ice cloud tops at a given temperature is equal to the relative humidity at water saturation multiplied by a scale factor ($f_{ws} < 1$). It was shown that the temperature at which the ice vapor growth rates display a maximum is determined by this scale factor. Adjusting the scale factor so that the maximum in ice vapor growth rates matches the maximum in effective radius inferred over the tropics leads to a remarkable agreement between the vertical variation of retrieved average effective radius and vapor growth rates. Moreover, the maximum retrieved effective radius over ocean occurs at warmer cloud tops compared to over land, dictating a slightly larger scale factor over ocean, consistent with moister conditions generally over oceans.

However, the analysis of VD2020 was limited to a qualitative comparison of the relative vertical variation of ice crystal properties averaged over large areas and long time periods and the relative vertical variation of vapor growth rates estimated as described above. Here we turn to airborne remote sensing observations of subtropical convective clouds with a spatial resolution of about 50-100 m, combined with reanalysis data of relative humidity and temperature to estimate vapor growth rates at individual cloud tops. Similarly to VD2020, multi-angle polarimetric and radiometric measurements are use to infer ice effective radius, the aspect ratio of hexagonal components of crystals and a crystal distortion parameter are retrieved, from which the asymmetry parameter is in turn derived. This dataset allows to quantitatively relate the retrieved ice effective radius and other ice microphysical properties to cloud top temperature and humidity in super- and sub-saturated conditions over land and ocean. In addition, a conceptual effective radius growth model is constructed to interpret the observational results.

In section 2 we present the data, after which the conceptual model and observational results are presented in sections 3 and 4. We conclude the paper in section 5.

2 Data and methods

The remote sensing and atmospheric state data used here are obtained during the Studies of Emissions and Atmospheric Composition, Clouds and Climate Coupling by Regional Surveys (SEAC^{4}RS) campaign in 2013 (Toon et al., 2016). SEAC^{4}RS was based in Houston, Texas and targeted the continental United States and the Gulf of Mexico. Data are selected from flights conducted on August 21 and 30 and September 2, 4, 11, 13, 16, 18, and 22 by NASA's ER-2 aircraft, which operates at a nominal altitude of about 20 km. Flight legs in convective cloud regimes are selected based on visual inspection of Cloud Physics Lidar (CPL) profiles and Geostationary Operational Environmental Satellite system (GOES) imagery. Days with substantial influence of apparent advected outflow of mesoscale systems over land are avoided. In this study, a total of 14826 RSP footprints that meet the selection criteria discussed below are included, of which 42% are obtained over ocean (Gulf of Mexico) and the remainder over the southern United States. The data over land and ocean span the latitude ranges 29.6°N–37.7°N and 23.7°N–30.7°N, respectively.

Cloud properties are inferred from data of the Research Scanning Polarimeter (RSP Cairns et al., 1999, 2003). The RSP observes total and polarized reflectances from the visible to the shortwave infrared at 152 different viewing angles along the aircraft track. RSP's field of view is about 14 mrad, leading to pixel sizes of about 50–100 m for aircraft-cloud separations between 4 and 8 km. Interference of liquid clouds is avoided by only selecting RSP pixels for which no cloudbow, originating from scattering on spherical liquid particles, could be detected. In practice, a liquid index (LI) is computed from the RSP multi-directional polarization measurements as described by van Diedenhoven, Fridlind, et al. (2012), and only cases with $LI < 0.3$ are included.

Cloud top heights are determined from RSP's multi-directional reflectances using a multi-angular parallax technique (Sinclair et al., 2017). Median differences between cloud top heights derived from RSP and colocated CPL measurements during SEAC^{4}RS were found to be about 500 m (Sinclair et al., 2017).

Ice crystal shape characteristics and asymmetry parameters are retrieved from the polarized reflectances at 0.865 μm per the method described by van Diedenhoven, Cairns, et al. (2012); van Diedenhoven et al. (2013, 2020). This method retrieves the average aspect ratio and distortion level of components of complex crystals that are present at the cloud top, as well as the corresponding scattering asymmetry parameter (van Diedenhoven, Cairns, et al., 2012; van Diedenhoven et al., 2016). The distortion parameter (Macke et al., 1996) is a proxy for randomization of the crystal shape caused by a number of factors such as large-scale crystal distortion and complexity, microscale surface roughness, and impurities within the crystals (Hong & Minnis, 2015; Liu et al., 2013, 2014; Neshyba et al., 2013; Panetta et al., 2016; Tang et al., 2017). Aspect ratio is defined as the prism length divided by prism width for hexagonal plate-like components and the inverse of that for column-like components, leading to aspect ratio values equal or below unity. Geometrically averaged aspect ratios are reported here as recommended by (van Diedenhoven et al., 2016), in addition to the percentage of results consistent with column-like rather than plate-like components.

Ice cloud optical thicknesses and ice crystal effective radii are retrieved from a combination of RSP's near-nadir visible and shortwave infrared measurements (Nakajima & King, 1990). Ice crystal effective radius r_{e} is defined as (Foot, 1988)

$$r_{\mathrm{e}} = \frac{3}{4}\frac{V_t}{A_t} = \frac{3}{4\,\rho_i}\frac{m_t}{A_t} \tag{1}$$

where V_t, A_t and m_t are the total volume, projected area and mass of the ice crystal distribution and ρ_i is the bulk ice density. For this retrieval we use observations at 2.25 μm in combination with those at 0.86 μm over ocean. Over land, 0.67 μm is used as the visible wavelength to avoid the vegetation albedo red edge.

As described by van Diedenhoven et al. (2014), for each instrument footprint an ice optical model is used that is consistent with the retrieved asymmetry parameter for that footprint. Only RSP pixels with an optical thickness above 5 are included in the analysis.

Profiles of relative humidity, large-scale vertical motion, temperature and pressure are obtained from the Goddard Earth Observing System Model Forward Processing (GEOS-FP) meteorological data assimilation system. These reanalysis data have a resolution of 0.25° across latitude and 0.3125° across longitude, which is about 25 km^2, while the vertical resolution is 50 and 25 hPa above and below 700 hPa, respectively. GEOS-FP profiles are provided every 3 hours and are sub-sampled along the ER-2 ground track.

3 Crystal growth rate model

The growth rate of a single crystal in terms of its mass m can be estimated using the expression (Pruppacher & Klett, 1997)

$$\frac{\delta m}{\delta t} \approx 4\pi\, f_c\, D_{\max}\, G\,(S_i - 1), \tag{2}$$

where S_i is the saturation ratio with respect to ice, $D_{\max}$ is the particle maximum dimension, and f_c is a nondimensional capacitance shape factor (here assumed to be 0.5). The function G has units of mass per unit time per unit length and accounts for thermal and vapor diffusion growth processes depending on temperature and pressure (Pruppacher & Klett, 1997) and is approximated here as detailed by van Diedenhoven et al. (2020). Here, the term $G(S_i - 1)$ is referred to as the normalized growth rate.

Using Equation 2 in combination with an empirical mass-dimension relationship allows to estimate the mass growth rate for a particle with a given mass for given normalized growth rate. Furthermore, the effective radius of a particle with a given mass can be estimate per Eq. 1 using a projected area-dimension relationship and assuming a monodisperse size distribution. Here we use coefficients and exponents for mass- and area-dimensional power laws given by van Diedenhoven, Fridlind, et al. (2012), which are applicable over a wide range of D_{max} for cloud ice. Using this approach we model the increase of particle effective radius with time. First, Eq. 2 is used to determine the mass growth rate for a given normalized growth rate and initial crystal size. Subsequently, the crystal is allowed to grow at this rate for a time interval Δt=0.1s after which the growth rate is updated corresponding to the resulting particle mass using Eq. 2. This process is iterated for a total growth time of one hour assuming various initial ice sizes and normalized growth rates and results are shown in Fig. 1a. It is apparent that the effective radius growth rate is largest for small sizes and crystals quickly grow to effective radii > 25 μm comparable to those observed at cloud tops. Furthermore, the sensitivity of effective radius to initial crystal size decreases as growth time increases. Hence, after a certain growth time, the relative variation of effective radius is mostly determined by the normalized growth rate. After a full, half and quarter hour of growth, Fig. 1b shows the increase of effective radius as a function of normalized growth rate. This concept model is meant to qualitatively illustrate the relation between effective radius and normalized growth rate, which is useful for the interpretation of our observational results. The quantitative relationship may be expected to depend on the capacitance shape factor, particle size distribution, mass- and area-dimensional relationship, among other factors.

4 Observational results

The number of RSP ice cloud observations within 500-m cloud top height bins over land and ocean surfaces is shown in Fig. 2. Similarly to previous observations (van Diedenhoven et al., 2020; Kubar et al., 2007) and model studies (Gasparini et al., 2021) of convective clouds, the number of observations peak at cloud top heights of around 12 km or 220 K, corresponding to the estimated level of neutral buoyancy (van Diedenhoven et al., 2016). Compared to over land, relatively more cloud tops occur below the homogeneous freezing level over ocean, which is likely related to the weaker convection over ocean.

The average ice microphysical properties within the 500-m cloud top height bins are shown in Figs. 1b-1f along with the standard deviations. The statistics are only calculated for bins containing at least 25 observations, leading to statistically robust, continuous profiles over land and ocean. The variation of ice crystal microphysical properties with cloud top height are largely consistent with those observed from satellite measurements in the tropics and mid-latitude presented by van Diedenhoven et al. (2020). Specifically, effective radius generally decreases with altitude for cloud top higher than 10 km. The rate of this decrease decreases for cloud tops higher than 12 km. A maximum in effective radius occurs at below 10 km, although few clouds with tops lower than 10 km are observed over land. Compared to over ocean, effective radii over land are found to be 3.7 μm smaller on average, also consistent with the findings of VD2020.

Crystal distortion and aspect ratio generally increase with increasing cloud top height, leading to asymmetry parameters decreasing with cloud top height. No substantial difference in these variables between land and ocean is found. As shown by VD2020, the minimum in aspect ratio at 7 km or 255 K corresponds to a minimum in the inherent growth ratios derived from laboratory observations and used in adaptive habit microphysics schemes to simulate crystal aspect ratios of vapor grown crystals (Hashino & Tripoli, 2011; A. A. Jensen et al., 2017). However, compared to the global results of VD2020, substantially lower aspect ratios, higher percentages of column-like crystal components

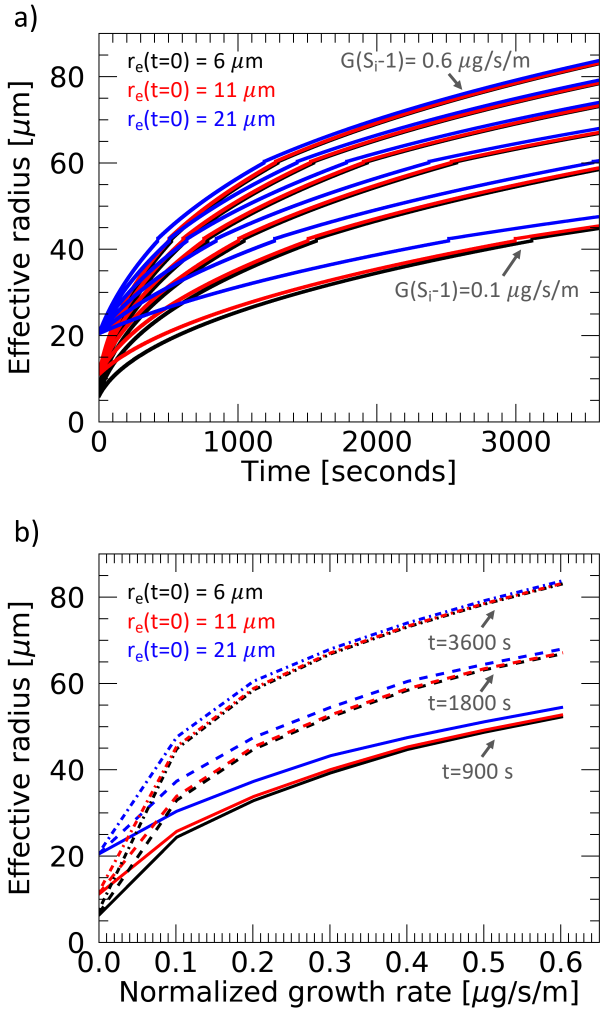

Figure 1. Single particle effective radius as a function of time (a) and normalized growth rate (b) as calculated using the simplified growth model described in section 3. Different colors represent different initial crystal sizes as indicated. The six clusters of lines in Panel a are for normalized growth rates in the range 0.1–0.6 $\mu g/s/m$ in equal steps. Different lines styles in Panel b represent different total growth times as indicated.

and larger asymmetry parameters are inferred during SEAC^{4}RS at this level, which may be attributable to the higher spatial resolution and less averaging.

The pressure, temperature and humidity profiles from reanalysis data colocated to the RSP footprints are used to calculate normalized vapor growth rate profiles as defined in section 3, which are subsequently interpolated to the cloud top level. While substantial variation of humidity may be expected within the 25 km^2 grid cell of GEOS-FP, it is assumed here that the normalized growth rate interpolated to the cloud top level is a reasonable representation of the average conditions at the cloud top surroundings. Table 1 and Fig. 3a show that, while most of the clouds have supersaturated conditions (i.e., positive normalized growth rates) at cloud top, the fraction of clouds with supersaturated conditions varies systematically with cloud top height and is generally smaller

Table 1. Number of observations and average values of observed parameters. Standard deviations are given in brackets. Values in bold indicate statistically significant differences between sub- and supersaturated conditions.

Parameter	Land		Ocean	
	sub-saturated	supersaturated	sub-saturated	supersaturated
Number	3629	5017	1070	5110
Cloud top height [km]	**11.7(1.8)**	**12.1(0.9)**	**11.8(2.4)**	**11.3(1.3)**
ω_{CT} [Pa/s]	**0.041(0.059)**	**-0.029(0.060)**	**-0.064(0.088)**	**-0.029(0.058)**
Effective radius [μm]	30.6(10.0)	30.9(10.9)	**36.5(8.3)**	**34.1(11.4)**
Asymmetry parameter	**0.750(0.034)**	**0.747(0.027)**	**0.741(0.049)**	**0.766(0.041)**
Distortion	0.634(0.133)	0.641(0.105)	**0.632(0.156)**	**0.578(0.146)**
Aspect ratio	0.449	0.464	0.475	0.438
Column percentage	14	13	**9**	**27**

over land compared to over ocean. For supersaturated conditions only, Fig. 3b shows the average normalized growth rates for 500-m cloud top height bins along with its standard deviation. Consistent to the findings of VD2020, the vertical variation of average normalized growth rates is similar to the vertical variation of effective radius seen in Fig. 2b, with normalized growth rates peaking near 8-9 km (242-253 K), decreasing with higher cloud top heights before leveling off above around 12 km. Furthermore, the normalized growth rates over ocean peak at a temperature that is about 2 km (7 K) higher than over land, similarly to as predicted by VD2020.

To further investigate the relationship between the normalized growth rates at cloud tops and the inferred ice microphysical properties, we calculate average ice properties in normalized growth rates bins of 0.025 μg/s/m width. A histogram of the normalized growth rates at cloud tops over land and ocean in shown in Fig 4a. For supersaturated conditions over land and ocean, Fig. 4b shows that the mean cloud top effective radii correlate significantly ($p < 0.01$) with normalized growth rates with Pearson correlation coefficients of 0.92 and 0.97, respectively. The relations over land and ocean are well described by linear fits with slopes of 43.4 and 43.2 and offsets of 26.7 and 25.5, respectively, if effective radius is in μm and normalized growth rates are in μg/s/m. Standard deviations do not vary substantially with growth rate and are given in Table 1. These relationships between effective radius and normalized growth rates resemble the modeled relationships presented in Fig. 1b. Specifically, the model suggests that crystals grow to have effective radii in the observed range within about 900 s, during which cloud heights would typically have increased by less than 1km (Heath et al., 2017).

For sub-saturated conditions, no correlation between negative growth rates and effective radius is seen, but a jump of about 10-40% is apparent in effective radii around zero growth rate. While ice mass is expected to decrease in sub-saturated conditions, sublimation primarily occurs at crystal edges, leading to rounding of the crystal and hence to a relatively strong decrease of the particle surface area (Nelson, 1998). As effective radii is determined by the ratio of mass over projected area (see Eq. 1), crystal rounding during sublimation may explain the lack of correlation between negative growth rates and effective radius and the increase of effective radius for sub-saturated conditions. For example, the effective radius of a spheroid is about 15% larger than that of a hexagonal prism of equal length and aspect ratio.

For the other ice microphysical properties, no strong correlations with positive (or negative) growth rates are seen. However, above ocean observed distortion levels, column percentages and asymmetry parameters differ significantly between sub-saturated and supersaturated cloud top conditions (see also Table 1). Specifically, larger distortion parameters are observed in sub-saturated conditions compared to supersaturated tops. This is consistent with laboratory observations of increased roughness structures forming on sublimating crystals (Pfalzgraff et al., 2010; Magee et al., 2014). Furthermore, lowest distortion parameters are found for supersaturated conditions with the lowest growth rates and a weak, but significant, increase of distortion with normalized growth rate is observed, which is consistent with laboratory studies finding crystal complexity increasing with growth rates (Schnaiter et al., 2016; Voigtländer et al., 2018). No significant difference in aspect ratios between sub- and supersaturated cloud tops are found, consistent with findings of (Nelson, 1998; Bailey & Hallett, 2004). However, column percentages are near zero for sub-saturated conditions, while larger and significantly increasing percentages are found for supersaturated conditions, which is consistent with the results by Bailey and Hallett (2004) and Schnaiter et al. (2016) at conditions colder than about 220 K. Furthermore, significantly lower asymmetry parameters are found for sub-saturated conditions, mostly associated with the larger distortion values.

In contrast, over land the differences in ice microphysical properties at cloud tops in sub-saturated versus supersaturated are generally not significant (see Table 1). Stronger variation in dynamics expected over land versus ocean may contribute to this contrast as crystals may be exposed to a larger range of thermodynamical conditions. Although vertical motion information at cloud scales is not available, the large scale vertical motions at cloud top ω_{CT} are derived from reanalysis profiles and indicate a clear contrast between land and ocean at sub-saturated cloud tops, with mean descending conditions over land and ascending tendencies at cloud tops over ocean (Table 1). Ascending conditions are found for supersaturated cloud tops over both land and ocean.

5 Conclusions

The presented dataset combining high-altitude aircraft-based remote sensing and reanalysis shows an approximately linear relationship with high correlation between normalized ice crystal vapor growth rates and effective radii at cloud top, further confirming previous conclusions by VD2020. Furthermore, the vertical variation of ice crystal aspect ratio and crystal distortion is similar to those shown by VD2020 and consistent with vapor growth processes. Significant differences in crystal shape characteristics and scattering asymmetry parameters are found between sub- and super-saturated cloud tops over ocean, although not over land. These observations further support the notion that the variability of ice crystal sizes and shapes at convective cloud tops may be controlled by the variability of vapor growth and sublimation processes.

The results suggest that ice particle distributions observed at cloud top have generally been subjected to depositional growth for a uniform amount of time at average conditions similar to the observed cloud top. Our conceptual model indicates that an ice crystal population may grow to have effective radii in the observed range at timescales during which cloud top heights and therewith cloud top conditions would not have changed substantially. A more complete model considering realistic air motions, particles size distributions and differential sedimentation may further inform about the relative importance of such processes (e.g., Krämer et al., 2016).

We further speculate that the variability of dynamical influences is stochastic and their signal in average properties largely cancels out. Greater variability of dynamics and humidity over land may be a plausible cause of the lower correlation of ice effective radius with growth rate and the lack of differences between ice properties of sub- and saturated cloud tops over land. Although no statistics of cloud scale vertical motion are available, a dynamical difference between land and ocean clouds is indicated by our finding that large scale vertical motion at cloud top levels for supersaturated conditions is ascending both over land and ocean, but at sub-saturated conditions, descending motion is observed on average at cloud tops over land, while ascending conditions are observed on average over ocean.

Our results are largely consistent with modeling results presented by E. J. Jensen et al. (2018) and Gasparini et al. (2021) demonstrating the importance of deposition growth in the evolution of the anvil cirrus. Furthermore, Muhlbauer et al. (2014) investigated observations of ice clouds evolved under a broad range of meteorological conditions, which indicate that variation in vertical velocity is a poor predictor for explaining the microphysical variability in ice clouds and suggest that the "variability in ice supersaturation and aerosols and their potential impacts on the availability of ice nuclei rather than variability in vertical velocity may be the primary drivers of the microphysical variability of midlatitude cirrus". However, we note that our results pertain to cloud top properties, while particle size sorting with height caused by differential fall speeds can largely determine the vertical variation of ice crystal sizes and shapes *within* clouds (E. J. Jensen et al., 2018). Additional processes, such as aggregation and riming likely lead to a even wider range of properties deeper within clouds. At cloud top, however, it may be expected that the primary process determining the vertical variation of effective radius and crystal shape is depositional vapor growth.

These results help interpretation of statistics of microphysical properties of ice crystals at cloud tops as generally observed by satellite measurements. Furthermore, the results provide valuable observational targets for studying ice formation and evolution processes using modeling studies. Cloud permitting modeling studies and other conceptual models that aim to reproduce and explain the observed vertical variation of ice microphysical properties at cloud top is advised as future work.

Acknowledgments
RSP and GEOS-FP data used in this paper is available at `https://espo.nasa.gov/seac4rs/content/SEAC4RS` (DOI: 10.5067/Aircraft/SEAC4RS/Aerosol-TraceGas-Cloud). Funding for this work is provided by NASA through grants NNX15AD44G (ACCDAM) and 80NSSC20M0224 (PACE-SAT). I would like to thank Dr. Ann Fridlind and Dr. Andrew Ackerman for their comments on earlier versions of this paper.

References

Bailey, M. P., & Hallett, J. (2004, mar). Growth Rates and Habits of Ice Crystals between 20 and 70C. *J. Atmos. Sci.*, *61*(5), 514–544. doi: 10.1175/1520-0469(2004)061⟨0514:GRAHOI⟩2.0.CO;2

Cairns, B., Russell, E. E., LaVeigne, J. D., & Tennant, P. M. W. (2003). Research scanning polarimeter and airborne usage for remote sensing of aerosols. *Proc. SPIE*, *5158*, 33–44. doi: 10.1117/12.518320

Cairns, B., Russell, E. E., & Travis, L. D. (1999). Research Scanning Polarimeter: calibration and ground-based measurements. *Proc. SPIE*, *3754*, 186–196.

Foot, J. S. (1988, jan). Some observations of the optical properties of clouds. II: Cirrus. *Q. J. R. Meteorol. Soc.*, *114*(479), 145–164. doi: 10.1002/qj.49711447908

Gasparini, B., Rasch, P. J., Hartmann, D. L., Wall, C. J., & Dütsch, M. (2021, February). A Lagrangian Perspective on Tropical Anvil Cloud Lifecycle in Present and Future Climate. *Journal of Geophysical Research (Atmospheres)*, *126*(4), e33487. doi: 10.1029/2020JD033487

Hashino, T., & Tripoli, G. J. (2011, jun). The Spectral Ice Habit Prediction System (SHIPS). Part III: Description of the Ice Particle Model and the Habit-Dependent Aggregation Model. *J. Atmos. Sci.*, *68*(6), 1125–1141. doi: 10.1175/2011JAS3666.1

Heath, N. K., Fuelberg, H. E., Tanelli, S., Turk, F. J., Lawson, R. P., Woods, S., & Freeman, S. (2017, apr). WRF nested large-eddy simulations of deep convection during SEAC4RS. *J. Geophys. Res.*, *122* (7), 3953–3974. doi: 10.1002/2016JD025465

Hong, G., & Minnis, P. (2015, apr). Effects of spherical inclusions on scattering properties of small ice cloud particles. *J. Geophys. Res.*, *120* (7), 2951–2969. doi: 10.1002/2014JD022494

Jensen, A. A., Harrington, J. Y., & Morrison, H. (2018, sep). Impacts of ice particle shape and density evolution on the distribution of orographic precipitation. *Journal of the Atmospheric Sciences*, *75* (9), 3095–3114. doi: 10.1175/JAS-D-17-0400.1

Jensen, A. A., Harrington, J. Y., Morrison, H., & Milbrandt, J. A. (2017, jun). Predicting Ice Shape Evolution in a Bulk Microphysics Model. *J. Atmos. Sci.*, *74* (6), 2081–2104. doi: 10.1175/JAS-D-16-0350.1

Jensen, E. J., van den Heever, S. C., & Grant, L. D. (2018, sep). The Life Cycles of Ice Crystals Detrained From the Tops of Deep Convection. *Journal of Geophysical Research: Atmospheres*, *123* (17), 9624–9634. doi: 10.1029/2018JD028832

Krämer, M., Rolf, C., Luebke, A., Afchine, A., Spelten, N., Costa, A., ... Avallone, L. (2016, mar). A microphysics guide to cirrus clouds – Part 1: Cirrus types. *Atmospheric Chemistry and Physics*, *16* (5), 3463–3483. doi: 10.5194/acp-16-3463-2016

Kubar, T. L., Hartmann, D. L., & Wood, R. (2007, nov). Radiative and convective driving of tropical high clouds. *J. Clim.*, *20* (22), 5510–5526. doi: 10.1175/2007JCLI1628.1

Liu, C., Lee Panetta, R., & Yang, P. (2013). The effects of surface roughness on the scattering properties of hexagonal columns with sizes from the Rayleigh to the geometric optics regimes. *J. Quant. Spectrosc. Radiat. Transfer*, *129*, 169–185. doi: 10.1016/j.jqsrt.2013.06.011

Liu, C., Yang, P., Minnis, P., Loeb, N., Kato, S., Heymsfield, A., & Schmitt, C. (2014, dec). A two-habit model for the microphysical and optical properties of ice clouds. *Atm. Chem. Phys.*, *14* (24), 13719–13737. doi: 10.5194/acp-14-13719-2014

Macke, A., Mueller, J., & Raschke, E. (1996). Single scattering properties of atmospheric ice crystals. *J. Atmos. Sci.*, *53* (19), 2813–2825.

Magee, N. B., Miller, A., Amaral, M., & Cumiskey, A. (2014, nov). Mesoscopic surface roughness of ice crystals pervasive across a wide range of ice crystal conditions. *Atm. Chem. Phys.*, *14* (22), 12357–12371. doi: 10.5194/acp-14-12357-2014

Muhlbauer, A., Ackerman, T. P., Comstock, J. M., Diskin, G. S., Evans, S. M., Lawson, R. P., & Marchand, R. T. (2014, apr). Impact of large-scale dynamics on the microphysical properties of midlatitude cirrus. *J. Geophys. Res.*, *119* (7), 3976–3996. doi: 10.1002/2013JD020035

Nakajima, T., & King, M. D. (1990). Determination of the optical thickness and effective particle radius of clouds from reflected solar radiation measurements. I - Theory. *J. Atmos. Sci.*, *47*, 1878–1893. doi: 10.1175/1520-0469(1990)047⟨1878:DOTOTA⟩2.0.CO;2

Nelson, J. (1998). Sublimation of Ice Crystals. *J. Atmos. Sci.*, *55* (5). doi: 10.1175/1520-0469(1998)055⟨0910:SOIC⟩2.0.CO;2

Neshyba, S. P., Lowen, B., Benning, M., Lawson, A., & Rowe, P. M. (2013, apr). Roughness metrics of prismatic facets of ice. *J. Geophys. Res.*, *118* (8), 3309–3318. doi: 10.1002/jgrd.50357

Panetta, R. L., Zhang, J.-N., Bi, L., Yang, P., & Tang, G. (2016). Light scattering by hexagonal ice crystals with distributed inclusions. *J. Quant. Spectrosc. Radiat. Transfer*, *178*, 336–349. doi: 10.1016/j.jqsrt.2016.02.023

Pfalzgraff, W. C., Hulscher, R. M., & Neshyba, S. P. (2010, mar). Scanning electron microscopy and molecular dynamics of surfaces of growing and ablating hexagonal ice crystals. *Atm. Chem. Phys.*, *10*(6), 2927–2935. doi: 10.5194/acp-10-2927-2010

Pruppacher, H. R., & Klett, J. D. (1997). *Microphysics of clouds and precipitation* (2nd ed.). Kluwer Academic Publishers.

Russotto, R. D., Ackerman, T. P., & Durran, D. R. (2016, mar). Sensitivity of thin cirrus clouds in the tropical tropopause layer to ice crystal shape and radiative absorption. *J. Geophys. Res.*(6), 2955–2972. doi: 10.1002/2015JD024413

Schnaiter, M., Järvinen, E., Vochezer, P., Abdelmonem, A., Wagner, R., Jourdan, O., ... Heymsfield, A. J. (2016, apr). Cloud chamber experiments on the origin of ice crystal complexity in cirrus clouds. *Atm. Chem. Phys.*, *16*(8), 5091–5110. doi: 10.5194/acp-16-5091-2016

Sinclair, K., van Diedenhoven, B., Cairns, B., Yorks, J., Wasilewski, A., & McGill, M. (2017, feb). Remote Sensing of Multiple Cloud Layer Heights using Multi-Angular Measurements. *Atm. Meas. Techn. Discuss.*, 1–23. doi: 10.5194/amt-2017-2

Tang, G., Panetta, R. L., Yang, P., Kattawar, G. W., & Zhai, P.-W. (2017). Effects of ice crystal surface roughness and air bubble inclusions on cirrus cloud radiative properties from remote sensing perspective. *Journal of Quantitative Spectroscopy and Radiative Transfer*. doi: 10.1016/j.jqsrt.2017.01.016

Toon, O. B., Maring, H., Dibb, J., Ferrare, R., Jacob, D. J., Jensen, E. J., ... Pszenny, A. (2016, May). Planning, implementation, and scientific goals of the Studies of Emissions and Atmospheric Composition, Clouds and Climate Coupling by Regional Surveys (SEAC^{4}RS) field mission. *Journal of Geophysical Research (Atmospheres)*, *121*(9), 4967-5009. doi: 10.1002/2015JD024297

Van Diedenhoven, B., & Cairns, B. (2020, apr). A flexible parameterization for shortwave and longwave optical properties of ice crystals and derived bulk optical properties for climate models. *Journal of the Atmospheric Sciences*, *77*(4), 1245–1260. doi: 10.1175/JAS-D-19-0193.1

van Diedenhoven, B., Ackerman, A., Fridlind, A., & Cairns, B. (2016). On averaging aspect ratios and distortion parameters over ice crystal population ensembles for estimating effective scattering asymmetry parameters. *J. Atmos. Sci.*, *73*(2), 775–787. doi: 10.1175/JAS-D-15-0150.1

van Diedenhoven, B., Ackerman, A. S., Fridlind, A. M., Cairns, B., & Riedi, J. (2020, mar). Global Statistics of Ice Microphysical and Optical Properties at Tops of Optically Thick Ice Clouds. *Journal of Geophysical Research: Atmospheres*, *125*(6). doi: 10.1029/2019JD031811

van Diedenhoven, B., Cairns, B., Fridlind, A. M., Ackerman, A. S., & Garrett, T. J. (2013, mar). Remote sensing of ice crystal asymmetry parameter using multi-directional polarization measurements – Part 2: Application to the Research Scanning Polarimeter. *Atm. Chem. Phys.*, *13*(6), 3185–3203. doi: 10.5194/acp-13-3185-2013

van Diedenhoven, B., Cairns, B., Geogdzhayev, I., Fridlind, A., Ackerman, A., Yang, P., & Baum, B. (2012). Remote sensing of ice crystal asymmetry parameter using multi-directional polarization measurements-Part 1: Methodology and evaluation with simulated measurements. *Atmospheric Measurement Techniques*, *5*(10), 2361–2374. doi: 10.5194/amt-5-2361-2012

van Diedenhoven, B., Fridlind, A. M., Ackerman, A. S., & Cairns, B. (2012). Evaluation of hydrometeor phase and ice properties in cloud-resolving model simulations of tropical deep convection using radiance and polarization measurements. *J. Atmos. Sci.*, *69*(11), 3290–3314. doi: 10.1175/JAS-D-11-0314.1

van Diedenhoven, B., Fridlind, A. M., Cairns, B., & Ackerman, A. S. (2014, oct). Variation of ice crystal size, shape, and asymmetry parameter in tops of tropical deep convective clouds. *J. Geophys. Res.*, *119*(20), 11,809–11,825. doi: 10.1002/2014JD022385

Voigtländer, J., Chou, C., Bieligk, H., Clauss, T., Hartmann, S., Herenz, P., ...

Ulanowski, Z. (2018, sep). Surface roughness during depositional growth and sublimation of ice crystals. *Atm. Chem. Phys.*, *18*(18), 13687–13702. doi: 10.5194/acp-18-13687-2018
Waliser, D. E., Li, J.-L. F., Woods, C. P., Austin, R. T., Bacmeister, J., Chern, J., … Wu, D. (2009). Cloud ice: A climate model challenge with signs and expectations of progress. *J. Geophys. Res.*, *114*(3), D00A21. doi: 10.1029/2008JD010015
Zelinka, M. D., Myers, T. A., McCoy, D. T., Po-Chedley, S., Caldwell, P. M., Ceppi, P., … Taylor, K. E. (2020, jan). Causes of Higher Climate Sensitivity in CMIP6 Models. *Geophysical Research Letters*, *47*(1). doi: 10.1029/2019GL085782

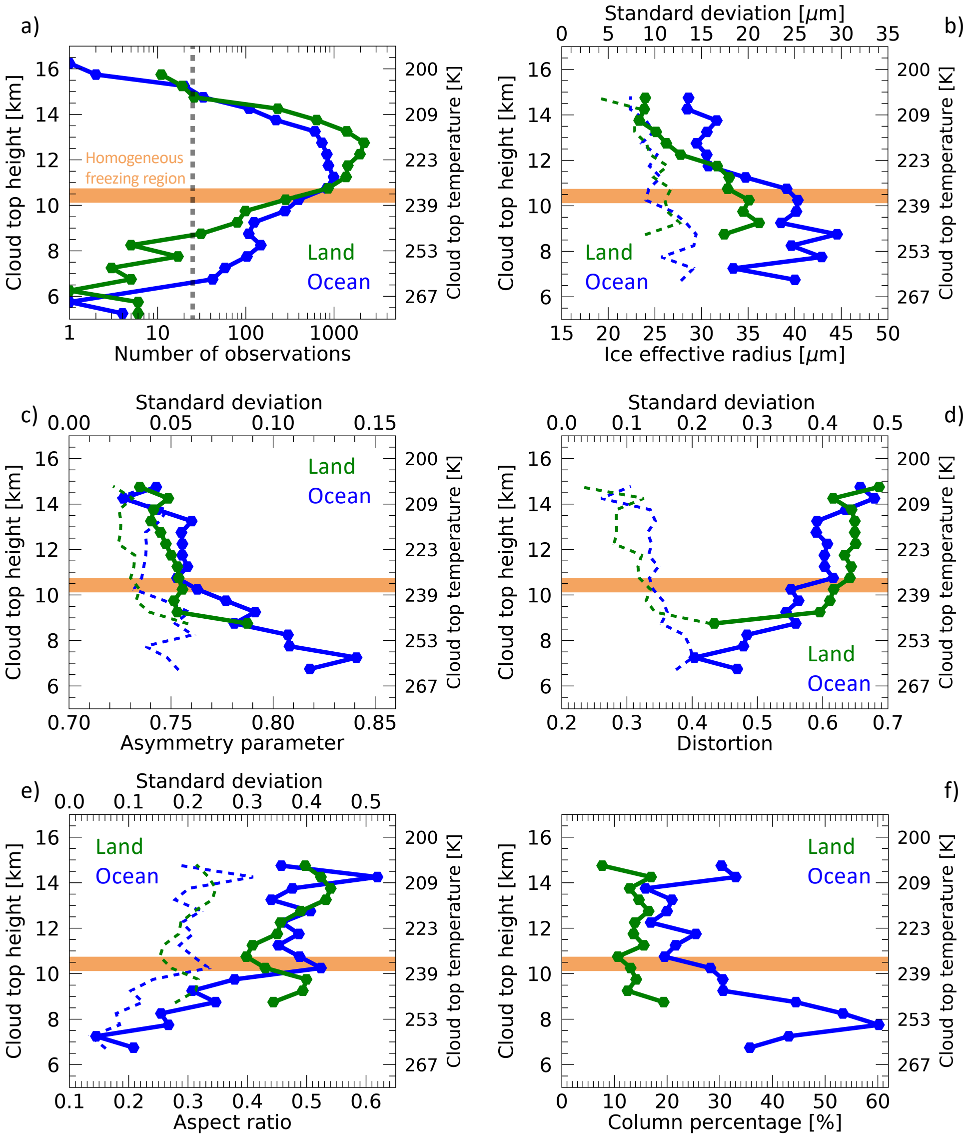

Figure 2. Total numbers (a) and average ice effective radius (b), asymmetry parameter (c), crystal distortion (d), aspect ratios (e) and percentage of column-like crystal components (f) in 500-m cloud top height bins over land (green) and ocean (blue). Dashed lines in panels (b-e) indicate the standard deviations (top axes). Statistics are only shown for cloud top height bins with at least 25 sampled, indicated by the grey dashed line in panel a. The brown bars indicate the region above homogeneous droplet freezing occurs.

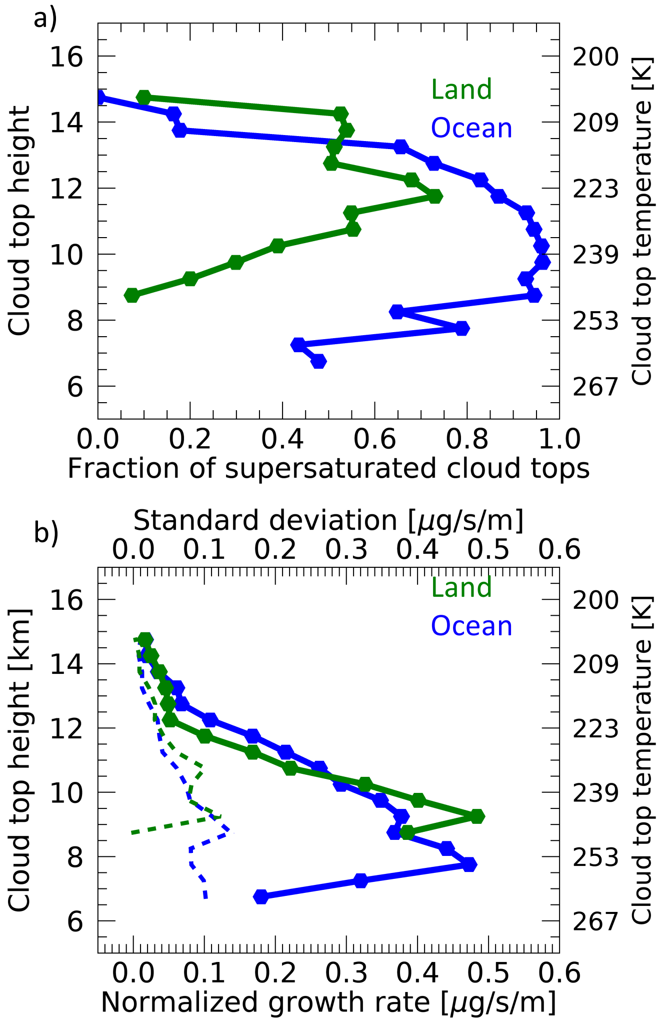

Figure 3. Panel a shows the fractions of supersaturated cloud tops (a) within 500-m cloud top height bins over land (green) and ocean (blue). Panel b shows the average (solid) and standard deviations (dashed) of the cloud top normalized growth rates within 500-m cloud top height bins.

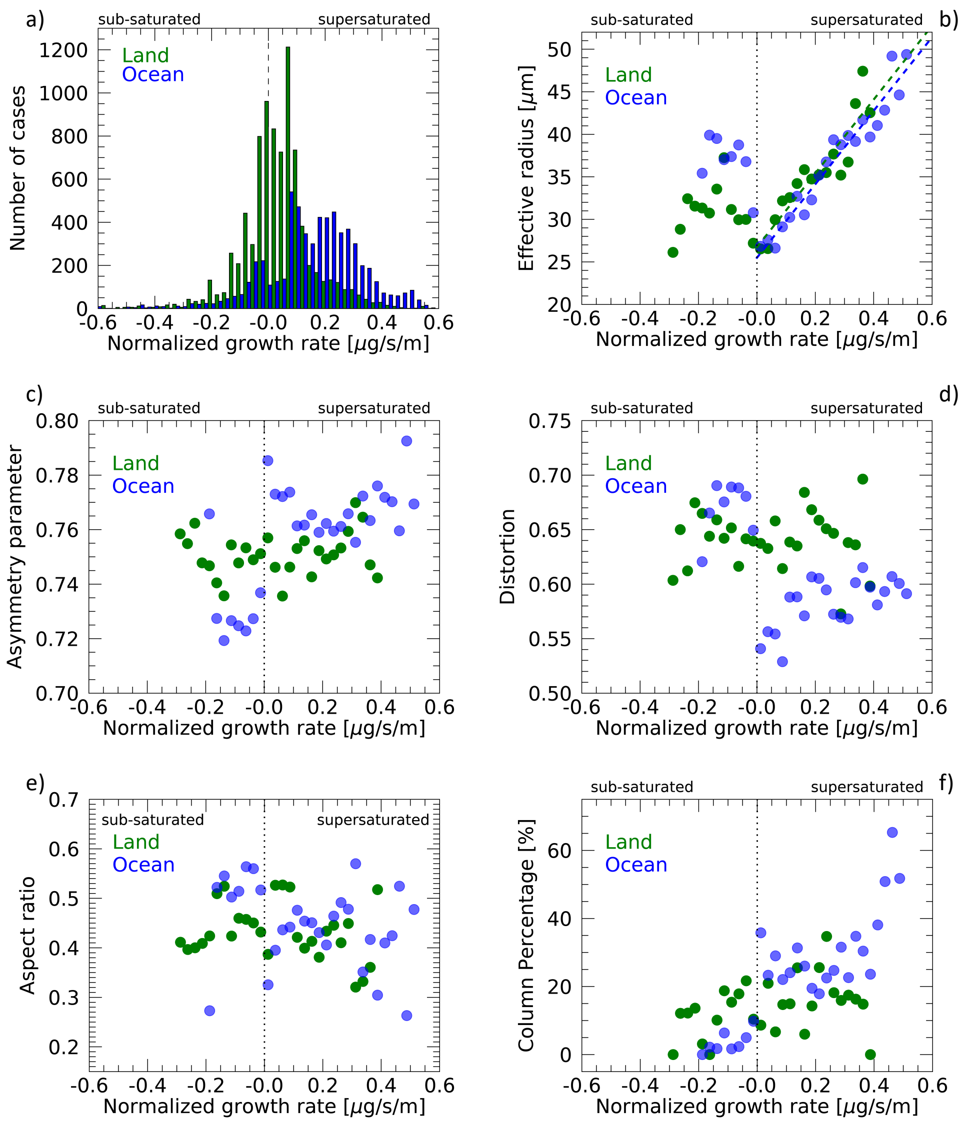

Figure 4. Total numbers (a) and average ice effective radius (b), asymmetry parameter (c), crystal distortion (d), aspect ratios (e) and percentage of column-like crystal components (f) in cloud-top normalized growth rate bins of 0.025 μg/s/m width over land (green) and ocean (blue). Linear fits to the data for supersaturated conditions are represented by dashed lines in Panel b.